

Co-pyrolysis of leather shaving waste and rice husk for hybrid palladium-supported biochar catalysts in hydrogenation reactions

Davide Baldassin^a, Lilia Longo^{a,*}, Federica Menegazzo^a, Carla Bittencourt^b, Mohsen Padervand^c, Michela Signoretto^a

^a CATMAT Lab, Department of Molecular Sciences and Nanosystems Ca' Foscari University of Venice and INSTM RUVe, Via Torino 155, 30172, Venezia Mestre, Italy

^b Chimie des Interactions Plasma-Surface, Université de Mons (UMONS), 20 Place du Parc, 7000, Mons, Belgium

^c Department of Chemistry, Faculty of Science, University of Maragheh, PO Box 55181-83111, Maragheh, Iran

ARTICLE INFO

Keywords:

Co-pyrolysis
Biochar
Catalysis
Leather
Rice husk
Hydrogenation
Benzaldehyde

ABSTRACT

The co-pyrolysis of tanned leather shaving waste (LS), a byproduct of the tanning industry, and rice husk (RH), an abundant agrifood residue, was performed to produce a hybrid activated biochar (ARL) to be used as support in the preparation of a Pd-based catalyst (Pd/ARL). The catalytic performance of Pd/ARL was compared with Pd/biochar catalysts derived from the pyrolysis of the individual feedstocks (Pd/ARH from rice husk and Pd/ALS from leather shaving) in the hydrogenation of benzaldehyde. Pd/ARH and Pd/ARL exhibited significantly higher initial activity, with turnover frequencies greater than Pd/ALS (1.41 s^{-1} and 0.58 s^{-1} vs. 0.09 s^{-1} , respectively). However, Pd/ALS and Pd/ARL demonstrated superior selectivity toward the desired product, benzyl alcohol (92 and 94 % for the former and later cases, respectively, vs. 78 % for Pd/ARH), effectively suppressing side reactions such as benzaldehyde acetalization with ethanol. Chemical and physical characterization of the biochars and catalysts revealed that Pd/ARL benefits from the synergistic properties of both feedstocks, including enhanced metal anchoring, high dispersion, and unique oxidation states. These factors contributed to the best overall catalytic performance, increasing the yield of desired products by up to 96 %. This research disclosed a novel strategy for the fabrication of cost-effective catalytic supports from waste materials aimed at modulating the hydrogenation reactions selectivity.

1. Introduction

The tannery industry transforms the byproducts of the meat processing industry into leather, a valuable and lasting product that is used in several fields [1]. The most common tanning agent is chromium, and up to days, 85 % of all leather produced in the world still relies on this process [2]. However, greener alternatives, such as vegetable tannins and green organic polymers, are emerging to eliminate the use of heavy metals in tanning [3]. Despite these advancements, leather production is renowned for the huge amount of toxic solid and liquid waste generated during the cleaning, fleshing, splitting, tanning, shaving, and buffing stages of raw materials [4], with an estimated production of 700 kg of solid waste per 1000 kg of wet salted leather [5]. The shaving residues consist of about 35–40 % of the waste, thereby representing a byproduct with significant environmental, economic, and disposal impacts. Thus, it is essential to develop efficient methods to transform these byproducts, mitigating the environmental issues associated with improper waste

management. Reusing waste materials, such as biomass and industrial by-products, has recently attracted huge attention, highlighting the significance of the circular economy in the new century. One approach for the biomass and waste conversion into value-added products is controlled pyrolysis, a thermochemical decomposition of organic matter in the absence of oxygen, which leads to the production of solid (biochar), liquid (bio-oil), and gaseous products (biogas) [6]. The pyrolysis of leather wastes has been investigated over the years [7], especially for char production and use in several applications, such as solid fuel [4], pollutants absorption and abatement [8,9], supercapacitors [10], batteries [11], and fertilizers [5,12]. However, European Union legislation limits the application of biochar from non-vegetable sources in fields such as fertilization, making it crucial to explore alternative, less-studied applications [13]. Recently, our research group explored the potential of an activated biochar derived from metal-free leather shaving waste (ALS), prepared using Life GOAST (Green Organic Agents for Sustainable Tanneries) technology as support for the heterogeneous catalysis of

* Corresponding author.

E-mail address: lilia.longo@unive.it (L. Longo).

<https://doi.org/10.1016/j.mtsust.2025.101127>

Received 31 January 2025; Received in revised form 21 March 2025; Accepted 26 April 2025

Available online 30 April 2025

2589-2347/© 2025 The Authors. Published by Elsevier Ltd. This is an open access article under the CC BY-NC-ND license (<http://creativecommons.org/licenses/by-nc-nd/4.0/>).

hydrogenation reactions [14,15]. However, ALS exhibited poor catalytic activity compared to the lignocellulosic-derived biochars. This was due to its low metal anchorage capacity and smooth morphology, adversely influencing inner cavities in charge of the mass transfer to the active sites. Despite these limitations, ALS displayed peculiar features, such as high surface area and N,O-functionalized surface, that could be advantageous to design efficient heterogeneous catalysts. Among various biomasses used for the heterogeneous catalyst fabrication, rice husk-derived activated biochar (ARH) showed superior performance as support for the Pd-based catalysts [15]. This was attributed to its hierarchical porous structure, which facilitates internal mass transfer, as well as good interaction and dispersion of the metal active sites on the surface [15]. Additionally, its hybrid nature, composed of both carbon and silica, further tuned its catalytic properties. In this work, the co-pyrolysis of leather shaving waste (LS) and rice husk (RH) has been explored to effectively modify the biochar properties, synthesizing a composite material that leverages the favorable attributes of both biomasses, resulting in an excellent-performance catalyst [16]. This approach has been previously reported for the co-valorization of lignocellulosic biomass with coal, plastics, or tire wastes [17], particularly to enhance the bio-oil yield and improve the quality of liquid fuel products [18], as well as optimization of the biochar features and physicochemical properties towards specific applications, such as soil amendament, water treatment etc. [19]. Co-pyrolysis can indeed tune the porosity, surface functionality, PZC, and surface charge of the final biochar [20]. The co-pyrolysis of rice husk with different biomasses or non-biomass wastes has already been investigated in the literature, targeting bio-oil [21] and biochar production [22–24]. For instance, the addition of rice husk to oily sludge was found to improve bio-oil quality due to the synergistic effect of the alkali ashes of the biomasses, which significantly reduced the oxygenated compounds [25]. In this regard, Zhang et al. [26] reported that the addition of rice husk to sewage sludge pyrolysis enhanced the aromaticity of the produced char and the immobilization of the heavy metals in the structure, thereby improving the removal efficiency. The co-pyrolysis of different types of leather waste has also been reported [27]. For example, the co-pyrolysis of tanned buffing dust, chrome shavings, and tanning sludges led to higher yields of light tar and increased surface area in the biochar. This improvement was attributed to the synergistic action of various metal compounds (like CaCO_3 and Fe_2O_3) in the residues [28]. However, the combination of leather shaving waste (LS) and rice husk (RH) for char production has not been reported yet.

In this work, co-pyrolysis and activation of LS and RH, resulting in the activated biochar labeled ARL, was investigated for the preparation of the Pd-based heterogeneous catalyst for the hydrogenation of benzaldehyde as industrially important reaction model. The activity of the obtained catalyst (labeled Pd/ARL) was compared to those derived from the single biomasses (Pd/ARH and Pd/ALS). A comprehensive characterization (CHNS, N_2 physisorption, Raman, XRD, pH_{PZC} , MP-AES, SEM, TEM, XPS, TPR, and CO Chemisorption) of the materials was carried out to elucidate the synergistic effects of the starting biomasses on the catalytic performance. The product selectivity was also explored in particular to highlight the crucial role of the support's physicochemical features on the reaction mechanism.

2. Experimental part

2.1. Biochars synthesis and activation

The biochars (BCs) were prepared by slow pyrolysis of two different biomasses, rice husks (RH) and the metal-free leather tannery shaving waste (LS), supplied by Riseria delle Abbadesse, Grumolo delle Abbadesse, and PASUBIO S.p.A., Arzignano, both in Italy, respectively. The biomasses underwent slow pyrolysis and steam activation. The detailed procedure can be found somewhere else [15]. Briefly, pyrolysis was performed in a vertical tubular oven equipped with a fixed bed quartz

reactor, maintained at 700 °C for 30 min with a heating rate of 5 °C/min and a nitrogen flow of 100 mL/min. The obtained BCs were subjected to an activation step with a mix of $\text{N}_2/\text{H}_2\text{O}$ (1:1 v/v) at a total flow rate of 100 mL/min, heated at 850 °C at a rate of 10 °C/min for 90 min, resulting in the corresponding activated biochars (ACs). For co-pyrolysis, RH and LS were ground to a mesh size lower than 100 μm and mixed in a 1:1 ratio (w/w) to give a homogeneous powder (RL), which was then subjected to the pyrolysis and activation processes under the same conditions. The BCs from rice husks, leather shaving waste, and co-pyrolysis were labeled BRH, BLS, and BRL, respectively. The corresponding ACs, labeled as ARH, ALS, and ARL, were washed with a 1 M HCl solution for 1 h using ultrasound to eliminate alkali ashes present in the feedstocks and then rinsed with deionized water until the chlorides were no longer detectable with an $\text{Ag}(\text{NO}_3)_2$ assay.

2.2. Preparation of the catalysts

The activated biochars were ground to a fraction of 63–40 μm . The catalysts were prepared by the deposition precipitation of H_2PdCl_4 (nominal 0.6 wt%) with a controlled pH of 10.5, which was adjusted over time with a NaOH solution (1 M). The mixture was stirred at room temperature for 2 h and then heated to 80 °C. At this temperature, a solution of sodium formate (2:1 with respect to Pd) was added, and the mixture was further stirred for another 1 h to form Pd^0 on the surface. The catalyst was then filtered and washed with deionized water until no chlorides, confirmed through a negative AgNO_3 test, then dried in an oven at 110 °C for 18 h. The obtained catalysts were labeled Pd/ARH, Pd/ALS, and Pd/ARL. The deposition precipitation method is recognized as a promising approach to prevent the formation of Pd oxychloride species on surface during the preparation of Pd catalysts, since such species negatively affect the hydrogenation performance of the catalysts by introducing acidity into the system [29].

2.3. Materials characterization

The BCs and ACs were analyzed using a CHNS elemental analyzer (UNICUBE, Elementar) to illustrate the chemical composition. The ash content was evaluated by thermogravimetric analysis (TGA 8000 PerkinElmer) following the ASTM-D7582 procedure. The oxygen % was calculated from the difference between the results of the two analyses, according to Equation (1).

$$\text{O}\% = 100 - (\text{C}\% + \text{H}\% + \text{N}\% + \text{S}\% + \text{Ash}\%) \quad (1)$$

Raman spectra were recorded using a micro-Raman system (Senterra Bruker Optik GmbH, Massachusetts, USA), $\lambda = 532 \text{ nm}$, and a laser power of 10 mW. The visible spectra were obtained using the Ocean Optics spectrophotometer (USB 2000), equipped with optical fiber, tungsten-halogen source, and silicon (350–720 nm) and germanium (720–1050 nm) detectors.

Scanning electron microscopy (SEM) was carried out using a FE-SEM LEO 1525 ZEISS (Jena, DE), equipped with the SE2 and InLens detectors, with an acceleration potential voltage of 15 keV. Samples were deposited on the conductive carbon adhesive tape and metalized by sputtering with chromium (8 nm).

X-ray powder diffraction (XRD) analysis was performed by a Bruker D8 Advance Da Vinci diffractometer equipped with a LynxEye detector and a sealed tube providing $\text{CuK}\alpha$ radiation at an accelerated voltage of 40 kV and an applied current of 30 mA.

The porosity properties were analyzed by N_2 physisorption at $-196 \text{ }^\circ\text{C}$ (Micromeritics Tristar Plus II) after a degassing treatment at 200 °C for 6 h at 0.15 mbar (Micromeritics VacPrep 061).

The point zero charge was determined by the pH drift method [30].

The XPS measurements were carried out with a PHI Genesis instrument from Physical Electronics (Chanhassen, MN, USA), equipped with a monochromatic $\text{Al K}\alpha$ X-ray source. The samples were supported on a copper conductive tape compatible with UHV for charge compensation.

Table 1
Ultimate analysis and the atomic ratio of ACs.

Sample	C [%]	N [%]	H [%]	S [%]	O [%]	Ash [%]	H/C	O/C
ALS	81.5	6.0	1.8	0.5	7.1	3.0	0.02	0.09
ARH	39.4	0.2	0.5	0.1	3.2	56.6	0.01	0.08
ARL	53.7	1.6	1.2	0.8	1.4	41.3	0.02	0.02

Dual charge neutralization was used to neutralize charge accumulation during analysis. The binding energy was calibrated based on the C 1s peak at 284.6 eV.

The samples were demineralized by refluxing for 5 h in a mixture of HCl:HNO₃:H₂O 3:1:4 and then subjected to Microwave Plasma Emission Spectrometry (Agilent Technology 4210 MP-AES) to quantify the Pd effective content.

Transmission electron microscopy (TEM) images were obtained using a Philips 208 TEM Microscope. The samples were prepared by putting one drop of an ethanol dispersion of the catalyst powder on a copper grid pre-coated with a Formvar film and drying in air.

Temperature Programmed Reduction (TPR), NH₃ Temperature Programmed Desorption (NH₃TPD), and CO chemisorption were carried out in lab-made equipment coupled with a Micromeritics TPRTD 2900 analyzer equipped with a Gow-Mac 24–550 TCD Detector (Bethlehem, PA, USA). For TPR analyses, 100 mg of the sample was placed in a U-shaped quartz reactor and heated from 25 to 800 °C with a rate of 10 °C/min in a reductive mixture of 5 % H₂ in Ar (40 mL/min). For NH₃TPD, 100 mg of the sample was placed in a U-shaped quartz reactor. The sample was first reduced by 5 % H₂/Ar mixture (30 mL/min) at 80 °C for 1 h. After cooling, it was exposed to a 5 % NH₃/He mixture (30 mL/min) at 25 °C for 1 h, followed by purging in He (30 mL/min) at for 1 h. The desorption was then performed in He (30 mL/min) with a temperature ramp of 10 °C up to 600 °C. For CO pulse chemisorption, 500 mg of the sample powders were placed in the same U-shaped quartz reactor, pre-treated in H₂ at 25 °C for 1 h, and then purged in He for 1 h. The system was then kept at 25 °C to inject 0.2 mL of CO through a loop until saturation.

2.4. Catalytic tests

Benzaldehyde hydrogenation was carried out in a semi-batch reactor consisting of a jacketed three-necked flask equipped with a hydrogen bubbler to flow the gas into the solution and a mechanical stirrer (IKA Eurostar). The reactor was connected to a thermostat (Thermo Scientific Haake DC 30) to maintain the temperature at 25 °C. The catalytic activity was measured in the hydrogenation of benzaldehyde under mild reaction conditions (25 °C and 1 bar) to ensure operation in the kinetic regime.

After preliminary tests to verify that the reaction was not affected by the mass transfer phenomenon, in a typical experiment, 200 mg of catalyst (mesh 63–40 μm) was placed in the reactor containing 75 mL of ethanol (Sigma Aldrich 99.8 %). H₂ was bubbled in the mixture with a flow rate of 30 mL/min at atmospheric pressure, and the system was heated at 80 °C for 1 h to ensure the complete reduction of Pd. The system was then cooled down to 25 °C, and benzaldehyde was added so that the final concentration became 0.1 M. The system was stirred at 1400 rpm and the reaction was monitored over time, sampling a small aliquot every 10 min. N-octane (Sigma Aldrich, 98 %) was used as an internal standard. The products were identified using a GC/MS (EI, 70 eV) with an HP5-MS capillary column (L = 30 m; Ø = 0.32 mm; film = 0.25 μm). The products were quantified by a gas chromatography instrument (Agilent Technologies 7820) equipped with an HP-5 column (L = 30 m, Ø = 0.32 mm, and film made of polysiloxane = 0.25 μm) coupled with an FID detector. The relative error of repeating the reactivity test for each catalyst was less than 5 %, and this was attributed to the instrumental error. For catalytic recycling, the operational

conditions were kept the same. Between the cycles, the catalyst was filtered and washed with ethanol and dried in the oven at 110 °C overnight.

Benzaldehyde conversion and the products selectivity were evaluated according to Equations (2) and (3):

$$\text{Conversion (\%)} = \frac{n_t \text{ Benzaldehyde} \cdot 100}{n_i \text{ Benzaldehyde}} \quad (2)$$

$$\text{Selectivity (\%)} = \frac{n_t \text{ product}}{n_i \text{ Benzaldehyde} - n_t \text{ Benzaldehyde}} \cdot 100 \quad (3)$$

Where n_i corresponds to the moles at the beginning of the reaction and not to the moles at different time intervals.

The kinetics constants and TOF values were also found using Equations (4) and (5), considering the reaction order of zero respect to benzaldehyde [31].

$$k_{\text{Benzaldehyde}} = \frac{dC_{\text{Benzaldehyde}}}{dt} \quad (4)$$

$$\text{TOF} = \frac{n_t \text{ products}}{n_{\text{Pd}} D_{\text{Pd}} \cdot t} \quad (5)$$

Where D_{Pd} corresponds to the Pd dispersion, calculated with CO chemisorption as: $D = \frac{N_s}{N_T}$. (N_s is the total number of metal atoms at the surface, and N_T is the total number of metal atoms (surface and bulk) [32]. The time considered for TOF calculation is 600 s.

3. Results and discussion

3.1. Materials characterization

Pyrolysis and activation of RH, LS, and RL were carried out on the feedstocks without any further pretreatment to preserve the natural inorganic species present in the biomass. It is well established that these species, in particular alkali metals, can catalyze both the pyrolysis process and activation step, enhancing the formation of pores and the high surface area [33,34]. The acidic washing was carried out after activation on the resulting ACs to remove the alkali metals that could influence the catalytic activity. Table 1 reports the elemental analysis, including ash and oxygen content, as well as the H/C and O/C ratios of the ACs after the acidic washing. Elemental analysis of the BCs before activation is reported in SI (Table S1). The obtained results revealed significant differences between the samples. ARH exhibited the lowest carbon content (39.4 %), due to the very high inorganic content (silica) of the biomass retained in the solid fraction after pyrolysis, activation, and even after acidic washing, and attributed to the silica present in the biomass [15]. ALS had the highest carbon content (81.5 %), while it was 53.7 % for ARL, confirming the contribution of the two biomasses in the final composition. ALS exhibited a very high percentage of heteroatoms (6 % N and 7 % O), deriving from the decomposition of the proteins composing the biomass (predominantly collagen) [35]. ARH had almost no nitrogen, while a small content (1.6 %) was retained in the co-pyrolyzed biochar. The oxygen content was lower in ARL compared to the other two materials, likely due to a promotion of oxygen removal during the co-pyrolysis, as reported in the literature [36]. According to the reports, a synergistic effect of the decomposition can occur in the co-pyrolysis of different materials (i.e., industrial sludges and biomass) because of the formation of oxygen-containing intermediates, the release of free radicals and due to the coexistence of different ashes that can act as catalysts, enhancing hydrogen transfer reactions and radicals formation. This results in the promotion of reactions such as deacetylation and decarbonylation, increasing oxygenated volatiles and condensates and, therefore, giving a lower amount of oxygen in the char [37,38]. Notably, all samples resulted in a low % of sulfur (>1 %) that could act as poison for the metal active phase [31]. The low O/C and

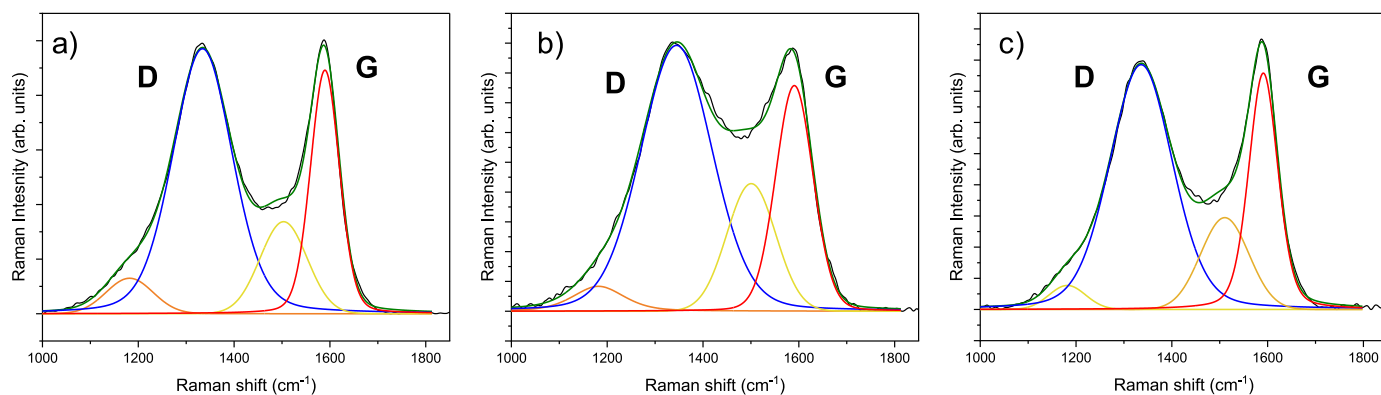


Fig. 1. Raman spectra of the activated biochars. a) ARH, b) ALS, c) ARL.

Table 2

Peak position of the D and G Raman bands, ID/IG ratios, and Full Width at Half Maximum (FWHM) of BCs and ACs.

Sample	D position (cm ⁻¹)	G position (cm ⁻¹)	ID/IG	FWHM D	FWHM G
BRH	1340	1588	0.90	148.6	88.2
ARH	1335	1589	1.09	148.6	70.5
BLS	1350	1580	0.98	186.4	110.8
ALS	1345	1590	1.18	176.4	93.2
BRL	1340	1588	1.03	148.6	78.1
ARL	1336	1592	1.03	156.2	73.1

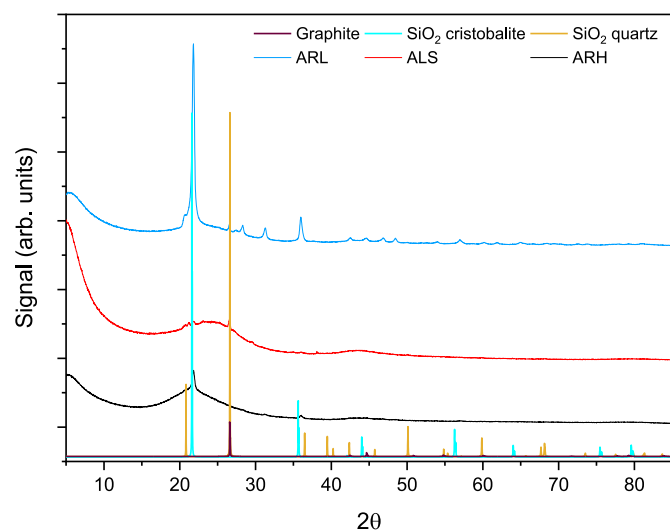


Fig. 2. XRD patterns of ARH, ALS, and ARL and reference patterns of quartz, cristobalite, and graphite.

H/C ratio, compared to other biochars reported in the literature [39–41], implies high degree of aromaticity.

The structural features of the chars were also investigated by Raman spectroscopy and XRD. In the Raman spectra of the biochars (Fig. S1) and the activated biochars (Fig. 1), two characteristic bands are present at around 1333 and 1590 cm⁻¹, which correspond to the sp²-bonded carbon with structural defects (D) and sp²-bonded graphitic carbon (G), respectively [39]. The peak position and values are given in Table 2. A few bands are also observed at 1180 and 1500 cm⁻¹, which can be due to some aromatics or volatile compounds still retained in the biochar structure [40]. The I_D/I_G ratio provides useful information about the order degree of the materials (Table 2). BRH showed a higher degree of order (0.90) compared to BLS and BRL (0.98, and 1.03, respectively).

After activation, the biochars obtained from the single pyrolysis displayed an increase in the structural defects due to the high-temperature treatment and the oxidative effect of steam [41]. At the same time, the I_D/I_G value for ARL was maintained. The presence of heteroatoms can cause a large number of defects in the carbon structure. Therefore, considering the elemental analyses, the Raman results are consistent with the O and N content in the ACs.

In the XRD patterns, Fig. 2, two broad peaks at 2θ = 22–25° (002) and 43° (110), are associated with the carbonaceous structure, based on the hexagonal graphite 2H model. These peaks correspond to the stacking of aromatic ring layers and the in-plane extension of aromatic molecules, respectively [14]. Compared to ordered graphite, where d (002) = 3.354 Å, the ACs exhibit a higher degree of disorder. ALS and ARL showed similar carbonaceous structures. Also, the results of XRD confirmed the presence of SiO₂ in various forms. In ALS apart from quartz as the most abundant phase, cristobalite and tridymite are also present. In ARH and ARL, on the other hand, cristobalite was typically detected for the sample derived from rice husk, as the prevalent form [42]. Notably, ARL shows a relatively higher abundance of SiO₂ compared to carbon, with the obvious predominance of the cristobalite phase. This evidenced once again that there are synergistic effects during the co-pyrolysis, enabling of promoting some specific reactions. Wang et al. [43], for example, found that the activation energy of co-pyrolysis of sludge and rice husk was lower than that of individual pyrolysis steps, allowing the reaction to proceed under milder conditions. This was attributed to the synergistic effects of alkali metals present in the biomasses [36]. Similar effects are expected to occur in the co-pyrolysis of RH and LS, influencing the reorganization of the silica crystal phase in the material and achieving a higher degree of order at an activation temperature of 850 °C.

From a morphological point of view, highlighted by SEM micrographs (Fig. 3), significant differences were evidenced for the obtained materials. ARH displayed a sponge-like structure made of deep cavities and holes with a diameter of some microns (<10 μm). It is reported that lignocellulosic biomasses are able to retain the shape of the plant cell walls, mainly made of cellulose, lignin, and hemicellulose [44], which could explain the peculiar structure of the AC. ALS instead showed a flatter morphology with some superficial cavities, probably due to the partial oxidation of the carbon caused by steam. The different nature of the shaving leather compared to lignocellulosic biomass, mainly made of collagen fibers, fibroblasts, and tanning agents [45], could explain the as-observed morphology. It is indeed made of soft matter that does not preserve its structure after pyrolysis. Looking at the SEM image of ARL, it is obvious that the cellular structure of the rice husk is somehow preserved. RH could act as a hard template for LS that instead melts completely under the pyrolysis conditions, forming a layer on the top of the rice husk biochar structure. According to previous works, the use of biopolymers like cellulose and starch and hard/soft templates (such as silica gel and self-assembly organic templates) results in interconnected

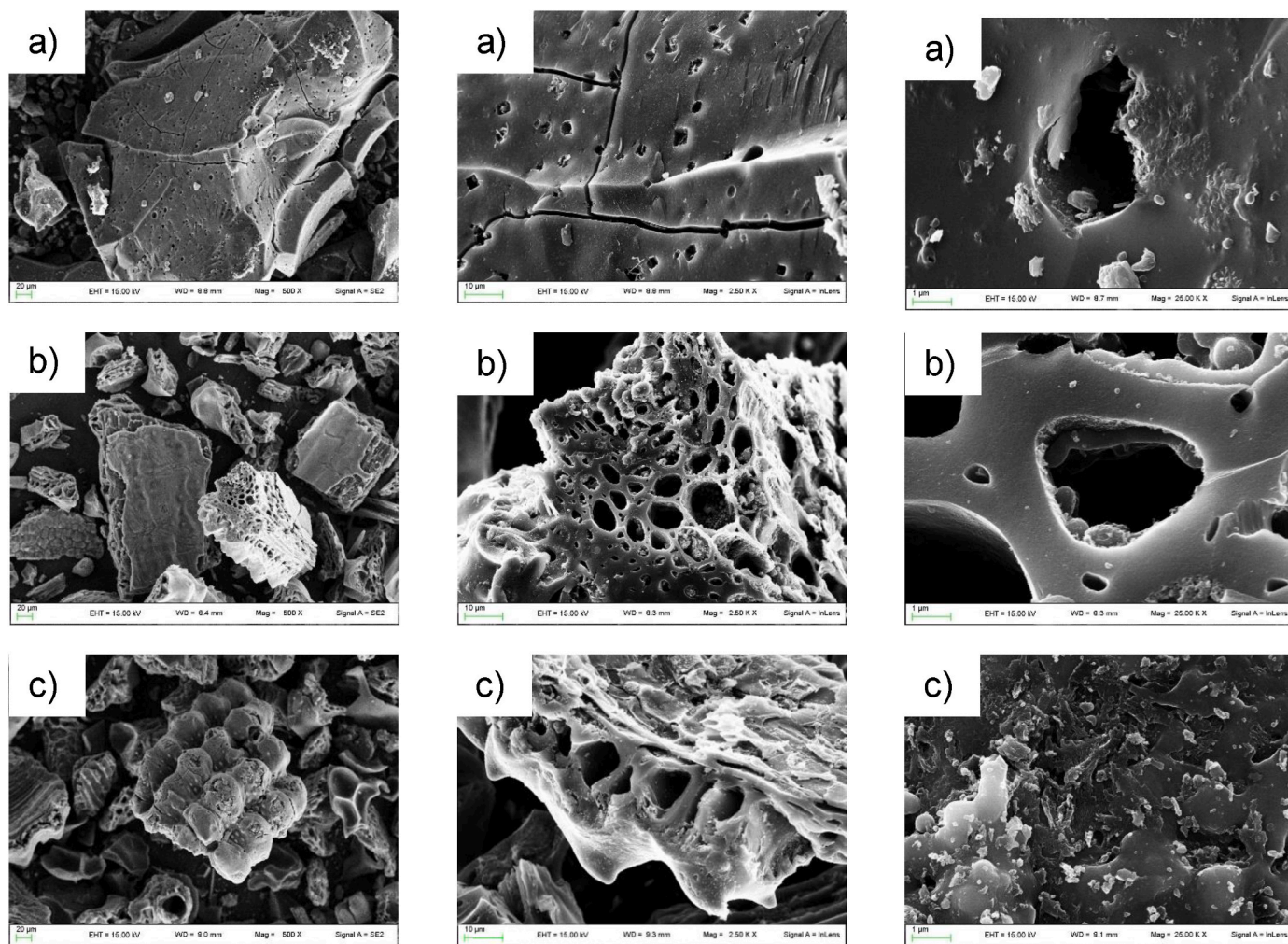


Fig. 3. SEM images at different magnifications of a) ARH, b) ALS, and c) ARL.

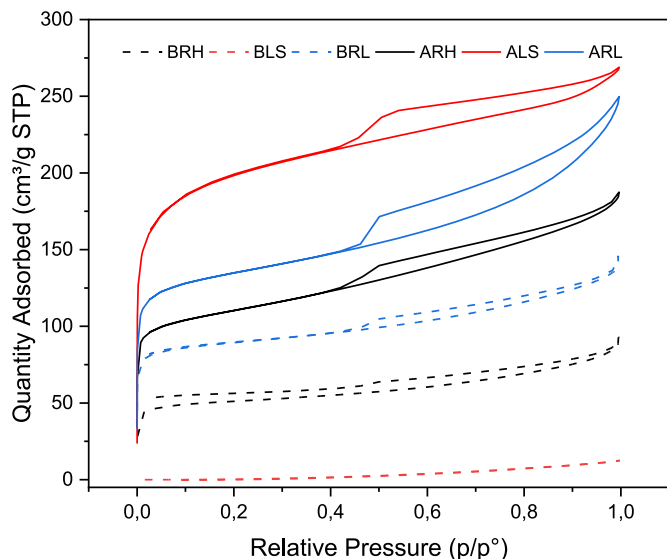


Fig. 4. N₂ adsorption-desorption of BCs (BRH, dashed red, BLS, dashed black, BRL dashed blue) and ACs (ARH solid red, ALS solid black, ARL solid blue).

Table 3
Textural properties of BCs and ACs.

Samples	S _{BET} (m ² /g) ^a	S _{Langmuir} (m ² /g) ^b	S _{micro} (m ² /g) ^c	V _{tot} (cm ³ /g) ^d	V _{micro} (cm ³ /g) ^e
BRH	199	323	270	0.15	0.06
BLS	/	/	/	/	/
BRL	345	438	271	0.13	0.10
ARH	378	489	375	0.14	0.10
ALS	684	907	563	0.23	0.12
ARL	445	618	463	0.17	0.12

structures consisting of micro, meso, and macro pores [46]. In this case, the natural hierarchical structure of lignocellulosic biomass is retained in ARL and acts as a hard template for the carbonization of LS. SEM images also confirm the similarity of Raman signals of ARL with ARH. The sponge-like structure of ARH and ARL is a key factor in catalysis because it can minimize the diffusive resistance to mass transport of the reactants on the surface of the catalyst [47].

N₂ physisorption analyses of BCs and ACs (Fig. 4, Table 3) were conducted to evaluate the textural properties. The adsorption-desorption isotherms of the BCs (dashed lines) show that the nature of the initial biomass influenced the final texture of the biochars. BLS resulted in a non-porous material, while both BRH and BRL displayed a porous pattern, confirming the analogies evidenced by SEM. Notably, BRL demonstrated the highest surface area, proving that there are synergistic effects occurring during the co-pyrolysis, that alter the final char

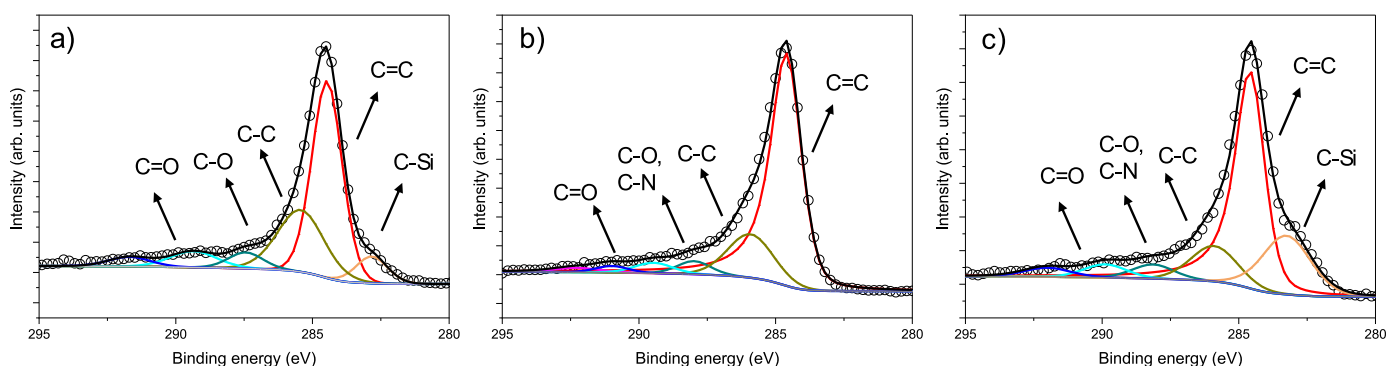
Table 4XPS atomic concentration and pH_{PZC} of ALS, ARH, and ARL.

Sample	XPS Atomic concentration [%]							pH_{PZC}
	C	O	N	Si	Ca	Cl	Na	
ALS	85.0	7.0	6.0	–	0.1	0.4	1.5	4.1
ARH	70.0	22.0	–	8.0	–	–	–	7.1
ARL	71.0	20.6	1.0	7.2	–	0.5	0.5	7.6

structure [43]. Wang et al. reported that during the co-pyrolysis of rice husk and sewage sludge, free radicals derived from the devolatilization of RH were formed, improving the contact frequency with the macromolecules of sewage sludge. Moreover, the presence of different alkali metals deriving from both biomass could catalyze the pyrolysis reaction, incrementing the volatilization and, therefore, promoting pores formation, modifying the texture of the final structure [48]. The activation step further increased the surface area of all materials. This was observed particularly in the case of ALS, which exhibited a $S_{Langmuir}$ of approximately 900 m^2/g and a typical isotherm type I, indicating a predominantly microporous structure. It is important to highlight that only the carbonaceous fraction undergoes modification during the activation. Therefore, BLS, having the higher C%, leads to the highest

carbon burn-off. Conversely, ARH and ARL displayed a combination of type I and type IV isotherms, with the coexistence of interconnected micro and mesopores. This difference is once again attributed to the natural characteristics of the starting feedstocks, and similar to the results of previous analyses, it confirms that rice husk played a major role in determining the structural and textural properties of ARL. It is known that high surface area is an important feature to achieve a good dispersion of the metal phase in catalysis. However, the interconnection of micro and mesopores is also of huge significance to facilitate the diffusion of reactants on the active sites.

The surface functionalities are another crucial feature that influences the catalytic activity through controlling the surface total charge and nucleation sites for metal nanoparticles growth. Table 4 illustrates the pH_{PZC} measured by the pH drift method, and the surface chemical composition of the materials, measured by XPS. The presence of C, N, O, Si on the surface of the samples alongside some traces of other inorganics like Ca, Na, and Cl was confirmed by XPS analyses. The high value of O atomic % reported for ARH and ARL (22 and 24 %, respectively) is mainly referred to the oxygen of SiO_2 . As depicted in Fig. 5, C1s core level spectra for ARH and ARL are deconvoluted into six contributions, while that of ALS gave five contributions. The main difference is related to the presence of the peak at 283 ± 0.6 eV, attributed to C–Si

**Fig. 5.** XPS spectra of a) ARH, b) ALS, and c) ARL.**Table 5**

C1s and N1s binding energies of ACs.

Sample	C1s (eV) (atomic %)						N1s (eV) (atomic %)		
	C–Si	C=C	C–C	C–O, C–N	C=O	π	Pyridinic	Pyrrolic	N-oxide
ARH	283.79 (9.89)	284.55 (67.50)	285.05 (8.86)	286.65 (5.50)	288.85 (4.39)	291.05 (3.85)	–	–	–
ALS	–	284.49 (61.97)	284.99 (17.41)	286.59 (10.32)	288.79 (5.48)	290.99 (4.82)	398.21 (32.8)	400.57 (56.0)	403.99 (11.2)
ARL	283.24 (13.14)	284.52 (58.53)	285.02 (12.24)	286.62 (6.84)	288.82 (4.93)	291.02 (4.31)	397.88 (34.6)	400.9 (65.4)	–

Table 6Catalytic activity for Pd/ACs on the hydrogenation of benzaldehyde. Reaction conditions: BAL 0.1 M, 100 mL EtOH, 200 mg catalyst, 25 °C, 1 bar H_2 30 mL/min, 1400 rpm.

Sample	TOF (s^{-1})	$k_{ald} \times 10^3$ ($mol L^{-1} s^{-1} gPd^{-1}$)	BAL conversion (%) at 30 min	BALOH yield (%) at 30 min	BALOH selectivity (%) at 30 min	BALOH + TOL yield (%) at 60 min
Pd/ARH	1.41	42	97	76	78	59 + 22
Pd/ALS	0.09	6	9	8	92	17 + 1
Pd/ARL	0.58	33	82	77	94	84 + 12

Table 7Pd effective wt.% measured by MP-AES, Pd NPs average size measured by TEM and CO chemisorption, Pd dispersion, and Pd $3d_{5/2}$ binding energies measured by XPS.

Sample	Pd effective wt.%	Average Pd particle size (nm)		Pd dispersion (D)	Pd $3d_{5/2}$ (eV) (atomic %)		
		TEM	CO chemisorption		–	–	–
Pd/ARH	0.64	1.2	4.1	0.26	334.20 (33)	335.96 (46)	337.74 (21)
Pd/ALS	0.44	1.8	2.3	0.47	–	335.78 (58)	337.59 (42)
Pd/ARL	0.67	1.5	2.1	0.53	–	335.70 (69)	337.52 (31)

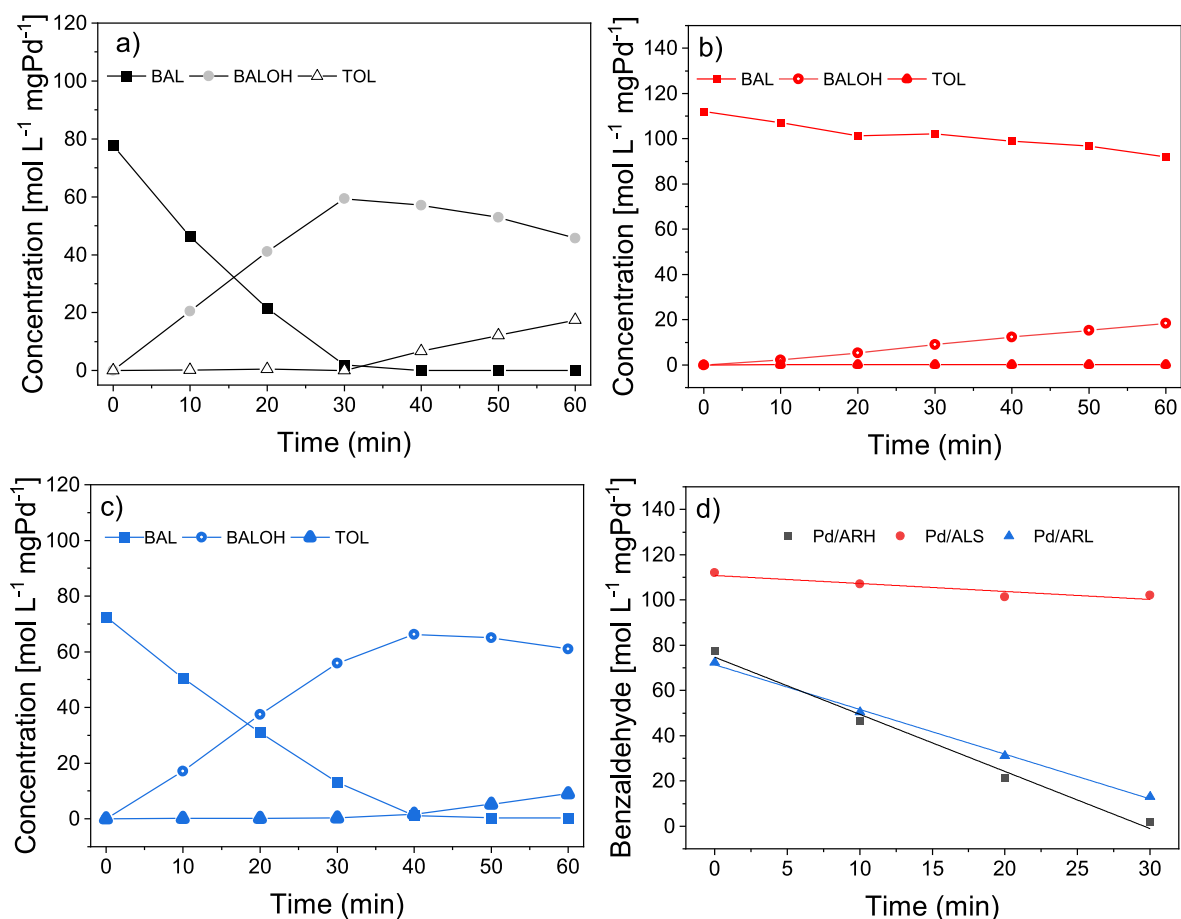


Fig. 6. Kinetic profiles of benzaldehyde hydrogenation over a) Pd/ARH, b) Pd/ALS, c) Pd/ARL and d) zero order plots. Reaction conditions: BAL 0.1 M, EtOH 100 mL, catalyst 200 mg, 25 °C, 1 bar H₂ 30 mL/min, 1400 rpm.

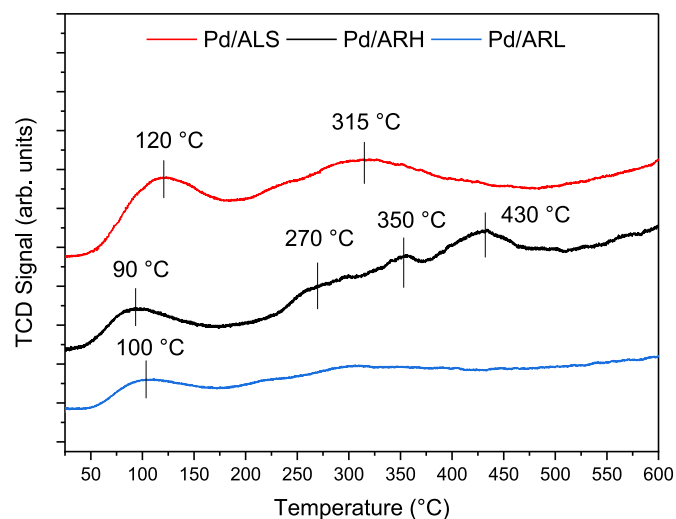


Fig. 7. NH₃ Temperature Programmed Desorption of the catalysts.

bonds [49,50]. The other components, at 284.5 ± 0.05 eV, 285.0 ± 0.05 eV, 286.6 ± 0.05 eV, 288.8 ± 0.05 eV and 291.0 ± 0.05 eV are assigned to sp^2 hybridization (C=C) of the graphitic and aromatic bonds, sp^3 C-C bonds, C-O or C-N, C=O, and π -plasmon excitations, respectively [51]. According to the atomic % of each contribution, as reported in Table 5, ALS has the highest amount of surface functionalities which can act as anchoring sites for metal NPs, with 10 % of

C-O/C-N species, in line with the chemical bulk composition reported by CHNS (Table 1). However, ARH and ARL also have a considerable amount of oxygen related to the SiO₂, that can be found in the form of -OH free functionalities on the surface. N1s core level spectra of A-LS (spectra reported in SI, Fig. S2, binding energies reported in Table 5) showed the presence of three main contributions at 398.2 eV and 400.6 eV, and 404.0 eV, that were attributed to pyridinic, pyrrolic and graphitic functionalities, respectively [52–54]. It is reported that pyridinic sites are the major contributors to the dispersion of metal NPs [54]. However, the presence of N-oxide groups, and C=O functionalities like carboxyl or carbonyl can also play an important role in modulating the charge of the material, increasing the overall acidity. An enhanced acidity of A-LS compared to the other biochars was confirmed by pH_{PZC} measurements, reported in Table 4 (the curves are reported in Fig. S3), that evidenced a low point zero charge (around 4.1) for ALS, compared to ARH and A-RL, which display neutral pH_{PZC}. The absence of N-oxide groups on the surface of ARL was considered the discriminant feature that decreased the acidity of the biochar obtained by co-pyrolysis.

3.2. Catalytic features and activity

MP-AES measurements were performed on the final catalysts to evaluate the effective Pd loading (Table 7). The analysis showed a lower effective wt. % for Pd/ALS compared to the other two samples (0.44 wt % vs. 0.64 wt% and 0.67 wt% for Pd/ARH and Pd/ARL, respectively). This difference can be attributed to the low PZC of ALS. Specifically, under the synthesis conditions employed, ALS, with a pH_{PZC} of 4, exhibits a significantly more negatively charged surface compared to ARH and ARL, which have a pH_{PZC} of approximately 7. This electrostatic

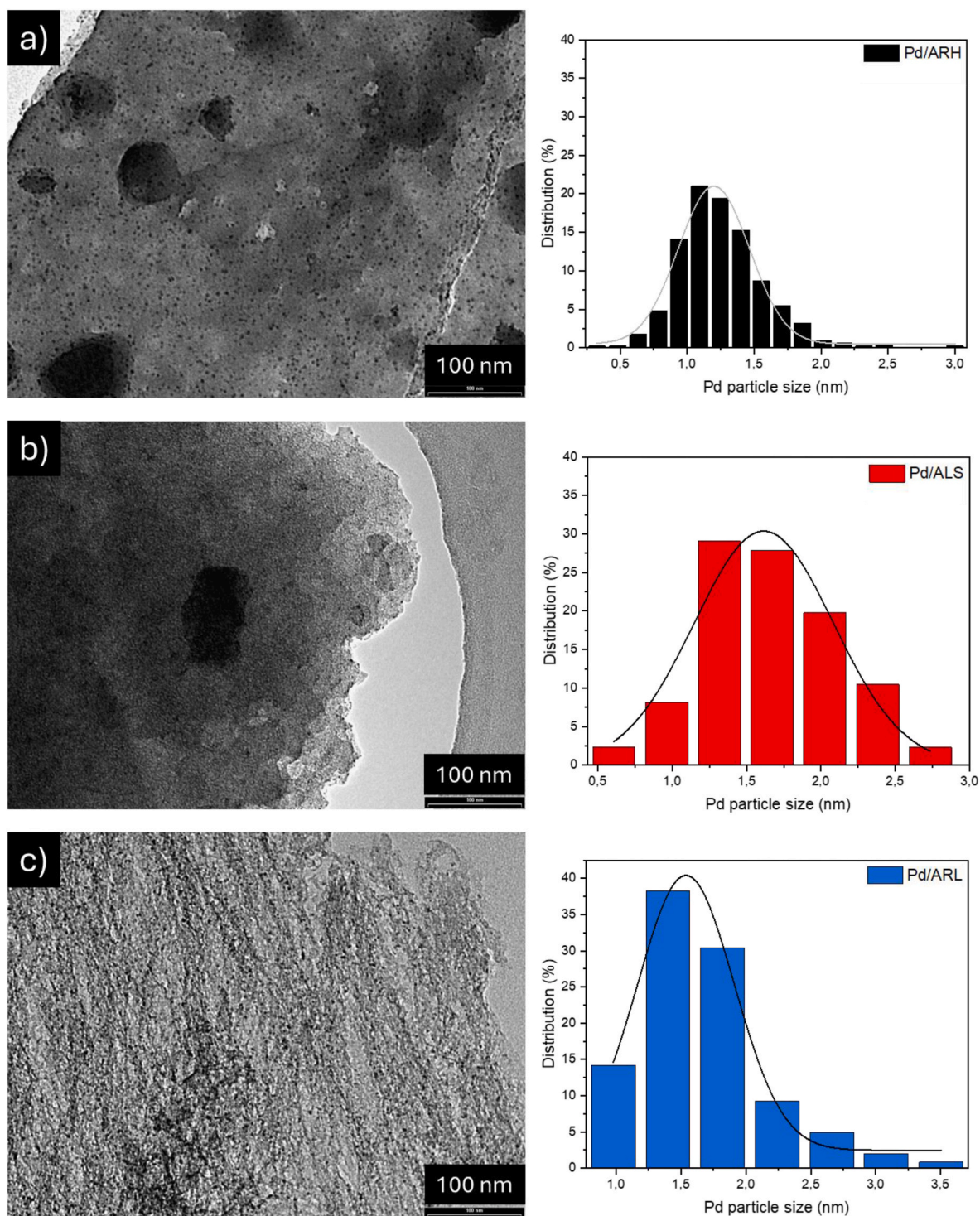


Fig. 8. TEM images and Pd particle size distribution of a) Pd/ARH, b) Pd/ALS, c) Pd/ARL.

environment could create conditions less conducive to the nucleation and growth of Pd nanoparticles, thereby resulting in less efficient deposition on ALS with respect to ARH and ARL. This difference was considered for the comparison of the catalytic tests results, normalizing the concentrations of the reactant and products by the gram of Pd effectively present in the reaction media.

Fig. 6 depicts the kinetic profiles for the consecutive hydrogenation of benzaldehyde to benzyl alcohol followed by the hydrodeoxygenation to toluene across the three catalytic systems. Zero-order plots [31] were compared to evaluate the kinetics of Pd over the different supports, and

the resulting kinetic constants for benzaldehyde conversion are reported in Table 6.

The catalytic activity of the systems were compared in terms of Turnover Frequency (TOF) [55], as detailed in Table 6, and revealed that Pd/ARH and Pd/ARL exhibited higher activity compared to Pd/ALS (1.41 and 0.58 s^{-1} , respectively, vs. 0.09 s^{-1}). Even though the TOF and k_{ald} of Pd/ARL with respect to Pd/ARH (33 vs. $42 \text{ mol L}^{-1}\text{s}^{-1}\text{mgPd}^{-1}$) were slightly lower, the yield of the desired products (BALOH and TOL) and consequently the selectivity was higher. The byproducts formed, especially over Pd/ARH, were identified as ethoxy and diethoxy

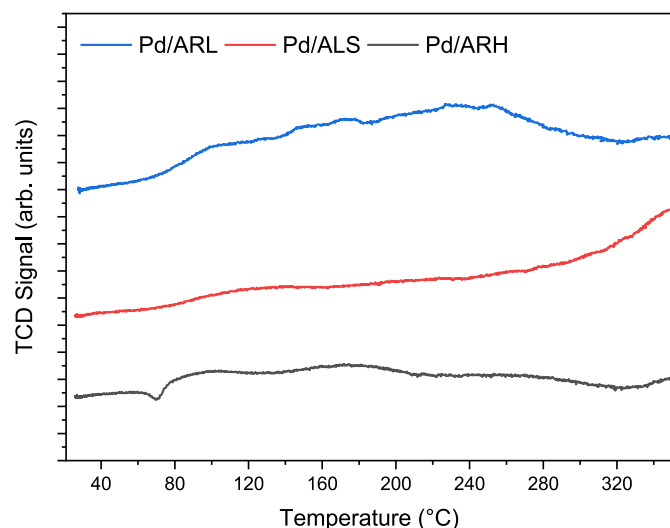


Fig. 9. Temperature Programmed Reduction of the catalysts.

methylbenzene, resulting from acetalization with ethanol used as the solvent [15]. While Pd/ARH exhibited higher activity, a portion of BAL was converted into byproducts, increasing the overall reaction rate and TOF without improving the hydrogenation product yield. The difference in catalytic activity of the samples was attributed to the chemical-physical properties of the supports which influenced the structural features of the final materials. NH_3 TPD analyses reported in Fig. 7 revealed that Pd/ARH had the highest acidity, with a peak at 120 °C, indicating the presence of weak acidity, and additional peaks, partially overlapping, at 270, 350, and 430 °C, indicating moderate and strong acid sites [56]. Pd/ALS displayed two distinct peaks (at 120 and 315 °C), corresponding to weak and medium acidity, however, the low % of Pd and activity, made it difficult to establish a direct correlation between acidity and catalytic performance. In contrast, Pd/ARL exhibited only a small peak at around 100 °C, related to weak acid sites, with no evidence of stronger acid sites. Consequently, Pd/ARL favored hydrogenation pathways, suppressing acid-catalyzed side reactions such as acetalization. Notably, catalyst acidity also plays a key role in the hydrogenolysis of BALOH to TOL, which explains the slower TOL formation observed with Pd/ARL compared to Pd/ARH (Fig. 6) [57].

TEM images (Fig. 8, S4, Table 7) evidenced that spherical Pd NPs were formed on the surface of all the catalysts, well-dispersed and with an average diameter <2 nm. However, Pd/ARH also exhibited larger and less uniform agglomerations with an average size of 22 nm (Fig. S4). This difference was corroborated by CO chemisorption measurements (Table 7), which indicated an average Pd NPs size of 4.1 nm for Pd/ARH, compared to 2.3 and 2.1 nm for Pd/ALS and Pd/ARL, respectively. Moreover, CO chemisorption indicated a higher Pd dispersion for Pd/

Table 8

Comparison of results obtained with different heterogeneous catalysts reported in literature.

Catalysts	Reaction conditions	TOF (h ⁻¹)	Ref.
0.67 wt % Pd/ARL		2088	This work
5 wt% Pt/MIL-101	50 mg cat., 21 mmol BAL, 20 mL ethanol, 25 °C 40 bar H ₂ .	4500	[77]
0.5 % Pd/C	4 mg Pd, 9.8 mmol BAL, 100 mL ethanol, 25 °C, 1 bar H ₂ .	1044	[31]
1.5 wt % single atom Pd/TiO ₂	0.2 μmol Pd, 0.5 mmol BAL, 10 mL ethanol, 30 °C, 1 bar H ₂	1002	[65]
0.95 wt % Pt/@-La ₂ O ₃ /SBA-15	100 mg cat., 1.88 mmol BAL, 20 mL H ₂ O, 40 °C, 7 bar H ₂	2324	[78]
5 wt % Pt on mesopolymer	12 μmol cat., 21 mmol BAL, 20 mL H ₂ O, 40 bar H ₂ , 25 °C	3462	[79]
1.1 wt % Au/Al ₂ O ₃	BAL/metal molar ratio: 1000, 0.05 M	234	[80]
0.7 wt % Pt/Al ₂ O ₃	BAL in H ₂ O, 80 °C, 9 bar H ₂	669	
1 % Pd/mayenite	25 mg cat., 2.4 mmol BAL, 10 mL diethyl ether, 20 °C, 8 bar H ₂	149.7	[70]
0.85 wt % Pt/@-ZrO ₂ /SBA-15	100 mg cat., 1.49 mmol BAL, 20 mL 2-propanol, 50 °C, 10 bar H ₂	2143	[81]
1 wt % Pd/GPN	BAL to metal molar ratio: 1000, 0.3 M BAL in p-xylene, 50 °C, 2 bar H ₂	2127	[82]

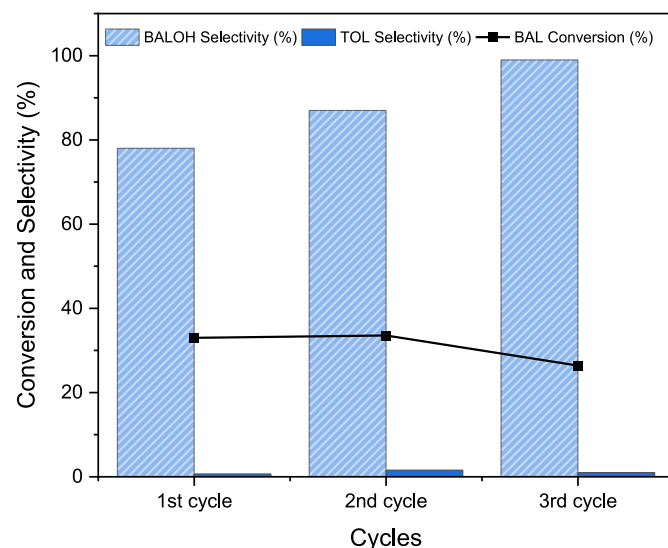


Fig. 11. Recycling cycles over Pd/ARL.

ARL (0.53), followed by Pd/ALS (0.47), and Pd/ARH (0.26). The presence of a negative peak at 80 °C in the TPR profile of Pd/ARH (Fig. 9), related to the decomposition of the β -hydride species [31], confirmed the presence of larger particles on the surface of Pd/ARH. The absence of

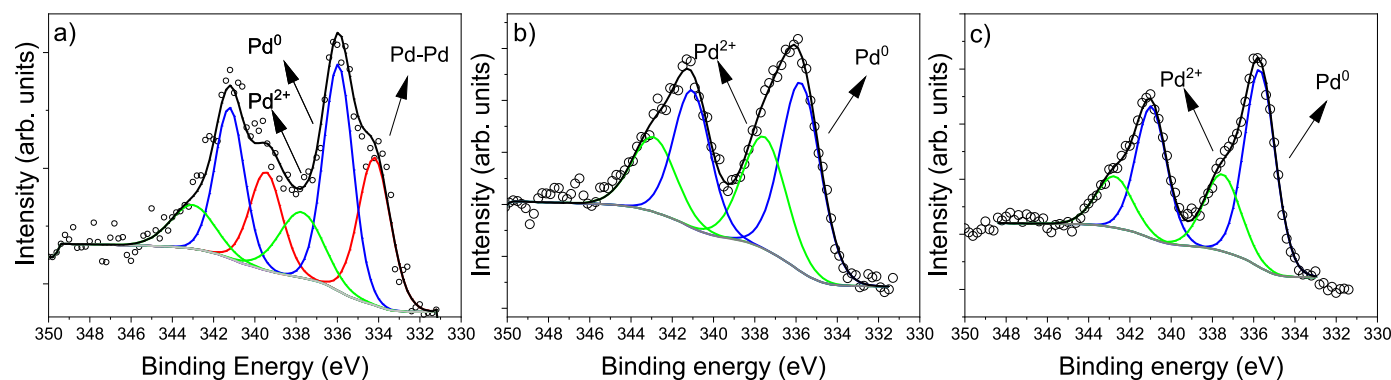


Fig. 10. XPS spectra of Pd 3d. a) Pd/ARH, b) Pd/ALS c) Pd/ARL.

this peak in Pd/ARL and Pd/ALS can be attributed to the formation of small (<2 nm) Pd nanoparticles and/or a low amount of Pd [58,59]. Notably, the absence of other peaks at higher temperature confirmed that the preparation method was successful to avoid the formation of oxychlorides species (typically reducing around 250 °C).

Apart from Pd size and distribution, it is well known that Pd⁰ is the most active phase in hydrogenation reactions [60]. Therefore, Pd3d XPS measurements were performed to assess the amount of Pd⁰ and Pd²⁺ on the surface of the catalysts (Fig. 10, Table 7). For Pd/ALS and Pd/ARL, the doublets corresponding to Pd 3d_{5/2} and Pd 3d_{3/2} were resolved into four distinct components, whereas six components were identified for Pd/ARH. Regarding Pd 3d_{5/2}, the predominant peak at 335.7 ± 0.2 eV was attributed to the metallic Pd⁰, while the shoulder at 337.6 ± 0.2 eV implies the presence of Pd²⁺ on the surface, likely in the form of PdO. The signal at 334.20 eV observed for Pd/ARH was associated with metallic Pd⁰ existing as larger nanoparticles, consistent with the previous characterization findings. It is known indeed that the 3d binding energy of Pd⁰ shifts towards higher values with decreasing cluster size [51]. The atomic surface concentration of the Pd species is summarized in Table 7. Notably, considering the double contribution of Pd⁰ for Pd/ARH, this sample exhibits the highest proportion of reduced species (approximately 80 %), followed by Pd/ARL (around 70 %) and Pd/ALS (about 60 %), confirming a positive relation between the oxidation states of the metal and the activity. The higher selectivity of Pd/ARL is therefore to be also referred to the more homogeneous distribution and higher dispersion of Pd. The high percentage of Pd²⁺ in Pd/ALS could be assigned to several factors. For instance, a greater presence of micropores on ALS can hinder the reduction of Pd species by limiting the accessibility and diffusion of the reducing agent to the active sites where Pd precursor are adsorbed [61]. Additionally, oxygen functionalities on the carbon surface play a significant role. It has been reported that oxygen functionalities, especially carboxylic groups, enhance H-spillover, promoting metal reducibility and increasing the catalytic activity [62]. However, Stucchi and coworkers [60] found that an excessive presence of highly polarized oxygen functionalities such as C=O, can hinder benzaldehyde hydrogenation by interfering with interactions between the aromatic ring and the catalytic surface, ultimately reducing catalytic efficiency. These two perspectives highlight the complex role of oxygen functionalities. In the case of Pd/ALS, the high amount of O-groups likely limited benzaldehyde adsorption, that combined with its lower metal loading, resulted in lower catalytic performance. Meanwhile, Pd/ARL benefited from an optimized balance of oxygen functionalities, enhancing the hydrogenation activity without hindering benzaldehyde adsorption on the catalyst's surface. Ultimately, the combination of several factors, including Pd oxidation state, metal dispersion, surface functionalities, micro- and mesoporosity, was crucial in optimizing Pd/ARL performance, making it a competitive catalyst, compared to other systems reported in literature (Table 8).

The hydrogenation of benzaldehyde is often reported as a model reaction to evaluate the activity of a catalytic systems in hydrogenation reactions, therefore extensive studies are reported in literature, investigating nobles and non-noble metals, oxides and carbon supports, mesoporous and microporous materials, and different reaction conditions [60,63–76]. To evaluate the catalytic properties of our systems, a comparison with the TOF of other catalysts was evaluated, in reaction systems as much similar as possible to the one employed in this work (liquid phase, mild reaction conditions), as reported in Table 8. The TOF registered for our system resulted in line with literature. Even if a higher initial activity is reported for other examples, often this is related to the use of expensive and complex systems. In our case the aim was to valorize a cost-effective waste that results complicated to be disposed.

Considering the promising results, Pd/ARL was subjected to recycling to assess the stability. The recyclability was investigated at less than 50 % conversion for three cycles, as reported in Fig. 11. After one cycle, the catalyst showed constant conversion and an increase in selectivity for both products (from 78 to 87 % for BALOH and from 0.9 to

1.8 % for toluene). The increased selectivity after one cycle can be attributed to the prolonged exposure of the catalyst to a constant flow of hydrogen, which may have enhanced the stability of the reduced Pd phase, thereby improving its efficiency in promoting the hydrogenation pathway. Ellis et al. reported that the selectivity of Pd catalysts for the hydrogenation of alkynes increased over time, due to the prolonged hydrogen exposure [83]. Despite a slight decrease of conversion after the third cycle (from 33 % to 26 %), the selectivity further increased, up to 99 % for BALOH and 1 % for toluene, achieving a higher total yield on the desired products (26.4 % after three cycles, compared to 25.9 % on the fresh catalyst).

4. Conclusions

The co-pyrolysis of leather shaving waste and rice husk proved to be an effective strategy to optimize the properties of the resulting biochar by integrating the complementary characteristics of the two precursors. The distinctive structure and morphology of RH were preserved, but the incorporation of LS significantly enhanced the surface area of the material, increasing S_{BET} from 378 m²/g (ARH) to 445 m²/g (ARL). Additionally, ARL exhibited a more functionalized surface with oxygen and nitrogen-containing groups (Table 5), compared to ARH which provided more nucleation sites for the metal phase, resulting in a higher dispersion (96.3 % increase in dispersion) and more uniform distribution of Pd nanoparticles.

The improved characteristics of Pd/ARL directly influenced its catalytic performance, achieving a hydrogenation product selectivity of 84 % for BALOH and 12 % for TOL and a TOF of 0.58 s⁻¹, while maintaining good stability over 3 reaction cycles. In contrast, Pd/ALS, with the smallest particle size (<2 nm) and good dispersion (47 %), suffered from poor metal anchoring due to the flat morphology and high microporosity of the support, indicated a lower activity. The limited activity was also caused by the existence of almost 50 % of Pd in the less-active Pd(II) state, reducing its efficiency for hydrogenation reactions.

The co-pyrolysis approach demonstrated tangible benefits in modifying the characteristics of single biochars. The limitations of RH alone, such as low surface area and poor functionalization, were mitigated by incorporating LS, resulting in ARL with enhanced textural and surface chemical properties. Similarly, the high microporosity and weak morphology of ALS were improved by the structural reinforcement from RH. These synergistic modifications addressed the negative characteristics of individual materials, making co-pyrolysis a promising strategy for designing effective biochar-based catalytic supports.

CRediT authorship contribution statement

Davide Baldassin: Writing – review & editing, Methodology, Investigation. **Lilia Longo:** Writing – original draft, Visualization, Investigation, Conceptualization. **Federica Menegazzo:** Writing – review & editing, Validation. **Carla Bittencourt:** Formal analysis, Data curation. **Mohsen Padervand:** Writing – review & editing, Validation. **Michela Signoretto:** Supervision, Resources.

Declaration of competing interest

The authors declare that they have no known competing financial interests or personal relationships that could have appeared to influence the work reported in this paper.

Acknowledgements

Alessandro Di Michele is acknowledged for the SEM and TEM analyses. Anssi Peuronen is kindly acknowledged for XRD analysis. The MIUR (Italian ministry for education, university and research) is gratefully acknowledged for the financial support (doctoral scholarships) of the inter-university Ph.D. program of University of Trieste and

University Ca' Foscari Venice. The European LIFE program LIFE GOAST – Green Organic Agents for Sustainable Tanneries (LIFE ENV/IT/000416) is acknowledged for the scientific work previously carried out. Conceria Pasubio S.p.A, Arzignano, Vicenza, and Riseria delle Abbadesse, Grumolo delle Abbadesse, Vicenza are acknowledged as well for the supply of the raw materials.

Appendix A. Supplementary data

Supplementary data to this article can be found online at <https://doi.org/10.1016/j.mtsust.2025.101127>.

Data availability

Data will be made available on request.

References

- [1] A. Mahmood Ali, A. Khan, M. Shahbaz, M. Imtiaz Rashid, M. Imran, K. Shahzad, A. Binti Mahpud, A renewable and sustainable framework for clean fuel towards circular economy for solid waste generation in leather tanneries, *Fuel* 351 (2023) 128962, <https://doi.org/10.1016/j.fuel.2023.128962>.
- [2] V.J. Sundar, J. Raghavarao, C. Muralidharan, A.B. Mandal, Recovery and utilization of chromium-tanned proteinous wastes of leather making: a review, *Crit. Rev. Environ. Sci. Technol.* 41 (2011) 2048–2075, <https://doi.org/10.1080/10643389.2010.497434>.
- [3] F. Chiampo, S. Shanthakumar, R. Ricky, G. Pattukandan Ganapathy, Tannery: environmental impacts and sustainable technologies, *Mater. Today Proc.* (2023), <https://doi.org/10.1016/j.matpr.2023.02.025>.
- [4] I.E. Onukak, I.A. Mohammed-Dabo, A.O. Ameh, S.I.R. Okoduwa, O.O. Fasanya, Production and characterization of biomass briquettes from tannery solid waste, *Recycling* 2 (2017) 17, <https://doi.org/10.3390/recycling2040017>.
- [5] K. Kuligowski, A. Cenian, I. Konkol, L. Świerczek, K. Chojnacka, G. Izydorczyk, D. Skrzypczak, P. Bandrów, Application of leather waste fractions and their biochars as organic fertilisers for ryegrass growth: agri-environmental aspects and plants response modelling, *Energies* 16 (2023) 3883, <https://doi.org/10.3390/en16093883>.
- [6] E. Muh, F. Tabet, S. Amara, Biomass conversion to fuels and value-added chemicals: a comprehensive review of the thermochemical processes, *Current Alternative Energy* 4 (2021) 3–25, <https://doi.org/10.2174/2405463103666191022121648>.
- [7] O. Yilmaz, I. Kantarli, M. Yuksel, M. Saglam, J. Yanik, Conversion of leather wastes to useful products, *Resour. Conserv. Recycl.* 49 (2007) 436–448, <https://doi.org/10.1016/j.resconrec.2006.05.006>.
- [8] K. Herrera, L.F. Morales, J.E. López, C. Montoya-Ruiz, S. Muñoz, D. Zapata, J. F. Saldarriaga, Biochar production from tannery waste pyrolysis as a circular economy strategy for the removal of emerging compounds in polluted waters, *Biomass Conversion and Biorefinery* 14 (2024) 22867–22880, <https://doi.org/10.1007/s13399-023-04261-2>.
- [9] Q. Li, Y. Tang, B. Zhou, J. Zhou, B. Shi, Resource utilization of tannery sludge to prepare biochar as persulfate activators for highly efficient degradation of tetracycline, *Bioresour. Technol.* 358 (2022) 127417, <https://doi.org/10.1016/j.biortech.2022.127417>.
- [10] B. Grycová, K. Klemencová, P. Leštinský, J. Stejskal, T. Saha, M. Trchová, J. Prokeš, Conductivity of carbonized and activated leather waste, *Sustain. Chem. Pharm.* 35 (2023) 101172, <https://doi.org/10.1016/j.scp.2023.101172>.
- [11] P. Salimi, S. Tieuli, S. Taghavi, E. Venezia, S. Fugattini, S. Lauciello, M. Prato, S. Marras, T. Li, M. Signoretto, P. Costamagna, R.P. Zaccaria, Sustainable lithium-ion batteries based on metal-free tannery waste biochar, *Green Chem.* 24 (2022) 4119–4129, <https://doi.org/10.1039/D1GC04772H>.
- [12] D. Skrzypczak, D. Szopa, K. Mikula, G. Izydorczyk, S. Baśladyńska, V. Hoppe, K. Pstrowska, Z. Wzorek, H. Kominko, M. Kulażyński, K. Moustakas, K. Chojnacka, A. Witek – Krowiak, Tannery waste-derived biochar as a carrier of micronutrients essential to plants, *Chemosphere* 294 (2022) 133720, <https://doi.org/10.1016/j.chemosphere.2022.133720>.
- [13] L_2021427IT.01014001.xml, (n.d.). <https://eur-lex.europa.eu/legal-content/IT/TXT/HTML/?uri=CELEX%3A32021R2088>.
- [14] L. Longo, S. Taghavi, E. Ghedini, F. Menegazzo, A. Di Michele, G. Cruciani, M. Signoretto, Selective hydrogenation of 5-hydroxymethylfurfural to 1-Hydroxy-2,5-hexanedione by biochar-supported Ru catalysts, *ChemSusChem* 15 (2022) e202200437, <https://doi.org/10.1002/cssc.202200437>.
- [15] L. Longo, S. Taghavi, M. Riello, E. Ghedini, F. Menegazzo, A. Di Michele, G. Cruciani, M. Signoretto, Waste biomasses as precursors of catalytic supports in benzaldehyde hydrogenation, *Catal. Today* 420 (2023) 114038, <https://doi.org/10.1016/j.cattod.2023.02.015>.
- [16] L. Wang, Y.S. Ok, D.C.W. Tsang, D.S. Alessi, J. Rinklebe, H. Wang, O. Mašek, R. Hou, D. O'Connor, D. Hou, New trends in biochar pyrolysis and modification strategies: feedstock, pyrolysis conditions, sustainability concerns and implications for soil amendment, *Soil Use Manag.* 36 (2020) 358–386, <https://doi.org/10.1111/sum.12592>.
- [17] H. Hassan, J.K. Lim, B.H. Hameed, Recent progress on biomass co-pyrolysis conversion into high-quality bio-oil, *Bioresour. Technol.* 221 (2016) 645–655, <https://doi.org/10.1016/j.biortech.2016.09.026>.
- [18] B.B. Uzojejinwa, X. He, S. Wang, A. El-Fatah Abomhara, Y. Hu, Q. Wang, Co-pyrolysis of biomass and waste plastics as a thermochemical conversion technology for high-grade biofuel production: recent progress and future directions elsewhere worldwide, *Energy Convers. Manag.* 163 (2018) 468–492, <https://doi.org/10.1016/j.enconman.2018.02.004>.
- [19] A. Al-Rumaihi, M. Shahbaz, G. Mckay, H. Mackey, T. Al-Ansari, A review of pyrolysis technologies and feedstock: a blending approach for plastic and biomass towards optimum biochar yield, *Renew. Sustain. Energy Rev.* 167 (2022) 112715, <https://doi.org/10.1016/j.rser.2022.112715>.
- [20] M.J. Ahmed, B.H. Hameed, Insight into the co-pyrolysis of different blended feedstocks to biochar for the adsorption of organic and inorganic pollutants: a review, *J. Clean. Prod.* 265 (2020) 121762, <https://doi.org/10.1016/j.jclepro.2020.121762>.
- [21] W.-H. Chen, K.-Y. Ho, R. Aniza, A.K. Sharma, A. Saravanakumar, A.T. Hoang, A review of noncatalytic and catalytic pyrolysis and co-pyrolysis products from lignocellulosic and algal biomass using Py-GC/MS, *J. Ind. Eng. Chem.* 134 (2024) 51–64, <https://doi.org/10.1016/j.jiec.2024.01.020>.
- [22] X. Wang, Z. Zhang, Z. Yan, Q. Li, C. Zhang, X. Liang, Synergistic contribution of metal–acid sites in selective hydrodeoxygenation of biomass derivatives over Cu/CoOx catalysts, *J. Colloid Interface Sci.* 648 (2023) 1–11, <https://doi.org/10.1016/j.jcis.2023.05.207>.
- [23] O.A. Fakayode, E.A.A. Aboagarib, C. Zhou, H. Ma, Co-pyrolysis of lignocellulosic and macroalgal biomasses for the production of biochar – a review, *Bioresour. Technol.* 297 (2020) 122408, <https://doi.org/10.1016/j.biortech.2019.122408>.
- [24] Y. Li, H. Yu, L. Liu, H. Yu, Application of co-pyrolysis biochar for the adsorption and immobilization of heavy metals in contaminated environmental substrates, *J. Hazard Mater.* 420 (2021) 126655, <https://doi.org/10.1016/j.jhazmat.2021.126655>.
- [25] B. Lin, Q. Huang, Y. Chi, Co-pyrolysis of oily sludge and rice husk for improving pyrolysis oil quality, *Fuel Process. Technol.* 177 (2018) 275–282, <https://doi.org/10.1016/j.fuproc.2018.05.002>.
- [26] J. Zhang, J. Jin, M. Wang, R. Naidu, Y. Liu, Y.B. Man, X. Liang, M.H. Wong, P. Christie, Y. Zhang, C. Song, S. Shan, Co-pyrolysis of sewage sludge and rice husk/bamboo sawdust for biochar with high aromaticity and low metal mobility, *Environ. Res.* 191 (2020) 110034, <https://doi.org/10.1016/j.envres.2020.110034>.
- [27] J. Zhang, G. Kang, H. Yang, Z. Liu, J. Yu, S. Gao, Co-pyrolysis kinetics and pyrolysis product distribution of various tannery wastes, *J. Fuel Chem. Technol.* 49 (2021) 1638–1647, [https://doi.org/10.1016/S1872-5813\(21\)60133-0](https://doi.org/10.1016/S1872-5813(21)60133-0).
- [28] J. Zhang, H. Yang, G. Kang, J. Yu, S. Gao, Z. Liu, C. Li, X. Zeng, S. Lu, The synergistic effect on the product distribution for the co-pyrolysis of tannery wastes, *Fuel* 322 (2022) 124080, <https://doi.org/10.1016/j.fuel.2022.124080>.
- [29] J.M. van Middlesworth, S.A. Wood, The stability of palladium(II) hydroxide and hydroxy–chloride complexes: an experimental solubility study at 25–85 °C and 1 bar, *Geochem. Cosmochim. Acta* 63 (1999) 1751–1765, [https://doi.org/10.1016/S0016-7037\(99\)00058-7](https://doi.org/10.1016/S0016-7037(99)00058-7).
- [30] Y.S. Al-Degs, M.I. El-Barghouthi, A.H. El-Sheikh, G.M. Walker, Effect of solution pH, ionic strength, and temperature on adsorption behavior of reactive dyes on activated carbon, *Dyes Pigments* 77 (2008) 16–23, <https://doi.org/10.1016/j.dyepig.2007.03.001>.
- [31] F. Pinna, F. Menegazzo, M. Signoretto, P. Canton, G. Fagherazzi, N. Pernicone, Consecutive hydrogenation of benzaldehyde over Pd catalysts: influence of supports and sulfur poisoning, *Appl. Catal. Gen.* 219 (2001) 195–200, [https://doi.org/10.1016/S0926-860X\(01\)00685-8](https://doi.org/10.1016/S0926-860X(01)00685-8).
- [32] G. Bergeret, P. Gallezot, Particle size and dispersion measurements, in: *Handbook of Heterogeneous Catalysis*, Wiley-VCH, 2008, pp. 738–765, <https://doi.org/10.1002/9783527610044.hetcat0038>.
- [33] Y.T. Kim, D.K. Seo, J. Hwang, Study of the effect of coal type and particle size on char–CO₂ gasification via gas analysis, *Energy Fuels* 25 (2011) 5044–5054, <https://doi.org/10.1021/ef200745x>.
- [34] P. Shrestha, D.D. Chun, K. Kang, A.E. Simson, N.B. Klinghoffer, Role of metals in biochar production and utilization in catalytic applications: a review, *Waste and Biomass Valorization* 13 (2022) 797–822, <https://doi.org/10.1007/s12649-021-01519-6>.
- [35] J. Kanagaraj, K.C. Velappan, N.K.C. Babu, S. Sadulla, Solid wastes generation in the leather industry and its utilization for cleaner environment-A review, *Journal of Scientific and Industrial Research* 65 (2006). <http://nopr.niscares.in/handle/123456789/4856>. (Accessed 26 November 2024).
- [36] J. Liu, X. Yang, H. Liu, X. Jia, Y. Bao, Mixed biochar obtained by the co-pyrolysis of shrimp shell with corn straw: Co-pyrolysis characteristics and its adsorption capability, *Chemosphere* 282 (2021) 131116, <https://doi.org/10.1016/j.chemosphere.2021.131116>.
- [37] Y. Liu, A. Ali Siyal, C. Zhou, C. Liu, J. Fu, Y. Zhang, B. Yao, L. Chao, H. Yun, J. Dai, X. Bi, Microwave co-pyrolysis of industrial sludge and waste biomass: product valorization and synergistic mechanisms, *Chem. Eng. J.* 485 (2024) 150032, <https://doi.org/10.1016/j.cej.2024.150032>.
- [38] X. Lin, Y. Guo, B. Tang, P. Fu, H. Li, J. Zhang, P. Li, Fast co-pyrolysis of paper mill sludge and corn stover: relationships between parameters, product distributions, and synergistic interactions, *Ind. Crop. Prod.* 213 (2024) 118415, <https://doi.org/10.1016/j.indcrop.2024.118415>.
- [39] J. Xu, J. Liu, P. Ling, X. Zhang, K. Xu, L. He, Y. Wang, S. Su, S. Hu, J. Xiang, Raman spectroscopy of biochar from the pyrolysis of three typical Chinese biomasses: a novel method for rapidly evaluating the biochar property, *Energy* 202 (2020) 117644, <https://doi.org/10.1016/j.energy.2020.117644>.

- [40] J. McDonald-Wharry, 2013–2014 Survey of Chars Using Raman Spectroscopy, *C* 7, 2021, p. 63, <https://doi.org/10.3390/c7030063>.
- [41] H. Li, Y. Liu, F. Jiang, X. Bai, H. Li, D. Lang, L. Wang, B. Pan, Persulfate adsorption and activation by carbon structure defects provide new insights into ofloxacin degradation by biochar, *Sci. Total Environ.* 806 (2022) 150968, <https://doi.org/10.1016/j.scitotenv.2021.150968>.
- [42] N. Prakongkep, R.J. Gilkes, W. Wiriyakitnateekul, A. Duangchan, T. Darunontaya, The effects of pyrolysis conditions on the chemical and physical properties of rice husk biochar, *Int. J. Mater. Sci.* 3 (2013) 97–103.
- [43] C. Wang, H. Bi, Q. Lin, X. Jiang, C. Jiang, Co-pyrolysis of sewage sludge and rice husk by TG-FTIR-MS: pyrolysis behavior, kinetics, and condensable/non-condensable gases characteristics, *Renew. Energy* 160 (2020) 1048–1066, <https://doi.org/10.1016/j.renene.2020.07.046>.
- [44] C.H. Pang, E. Lester, T. Wu, Influence of lignocellulose and plant cell walls on biomass char morphology and combustion reactivity, *Biomass Bioenergy* 119 (2018) 480–491, <https://doi.org/10.1016/j.biombioe.2018.10.011>.
- [45] J. Niu, R. Shao, M. Liu, Y. Zan, M. Dou, J. Liu, Z. Zhang, Y. Huang, F. Wang, Porous carbons derived from collagen-enriched biomass: tailored design, synthesis, and application in electrochemical energy storage and conversion, *Adv. Funct. Mater.* 29 (2019) 1905095, <https://doi.org/10.1002/adfm.201905095>.
- [46] C. Liang, Z. Li, S. Dai, Mesoporous carbon materials: synthesis and modification, *Angew. Chem. Int. Ed.* 47 (2008) 3696–3717, <https://doi.org/10.1002/anie.200702046>.
- [47] S. Dutta, A. Bhaumik, K.C.-W. Wu, Hierarchically porous carbon derived from polymers and biomass: effect of interconnected pores on energy applications, *Energy Environ. Sci.* 7 (2014) 3574–3592, <https://doi.org/10.1039/C4EE01075B>.
- [48] Q. Dai, Q. Liu, X. Zhang, L. Cao, B. Hu, J. Shao, F. Ding, X. Guo, B. Gao, Synergetic effect of co-pyrolysis of sewage sludge and lignin on biochar production and adsorption of methylene blue, *Fuel* 324 (2022) 124587, <https://doi.org/10.1016/j.fuel.2022.124587>.
- [49] M.Y. Bashouti, Y. Paska, S.R. Puniredd, T. Stelzner, S. Christiansen, H. Haick, Silicon nanowires terminated with methyl functionalities exhibit stronger Si-C bonds than equivalent 2D surfaces, *Phys. Chem. Chem. Phys.* 11 (2009) 3845–3848, <https://doi.org/10.1039/B820559K>.
- [50] T. Cai, X. Liu, J. Zhang, B. Tie, M. Lei, X. Wei, O. Peng, H. Du, Silicate-modified oiltea camellia shell-derived biochar: a novel and cost-effective sorbent for cadmium removal, *J. Clean. Prod.* 281 (2021) 125390, <https://doi.org/10.1016/j.jclepro.2020.125390>.
- [51] A. Felten, J. Ghijssen, J.-J. Pireaux, W. Drube, R.L. Johnson, D. Liang, M. Heccq, G. Van Tendeloo, C. Bittencourt, Electronic structure of Pd nanoparticles on carbon nanotubes, *Micron* 40 (2009) 74–79, <https://doi.org/10.1016/j.micron.2008.01.013>.
- [52] D. Polidoro, T. Chhabra, E. Rodríguez-Castellón, A. Perosa, R. Luque, D. Rodríguez-Padron, M. Selva, Pd-N-doped carbons for chemoselective hydrogenation of cinnamaldehyde: unravelling the influence of particle size and support in multiphase batch and continuous-flow systems, *Appl. Catal. Gen.* 685 (2024) 119864, <https://doi.org/10.1016/j.apcata.2024.119864>.
- [53] C. Varodi, F. Pogăcean, A. Ciorîță, O. Pană, C. Leostean, B. Cozar, T. Radu, M. Coros, R.I. Ștefan-van Staden, S.-M. Pruneanu, Nitrogen and sulfur Co-doped graphene as efficient electrode material for L-cysteine detection, *Chemosensors* 9 (2021) 146, <https://doi.org/10.3390/chemosensors9060146>.
- [54] X. Pan, X. Bao, The effects of confinement inside carbon nanotubes on catalysis, *Accounts of Chemical Research* 44 (2011) 553–562, <https://doi.org/10.1021/ar100160t>.
- [55] F. Schüth, M.D. Ward, J.M. Buriak, Common pitfalls of catalysis manuscripts submitted to chemistry of materials, *Chem. Mater.* 30 (2018) 3599–3600, <https://doi.org/10.1021/acs.chemmater.8b01831>.
- [56] F. Arena, R. Dario, A. Parmaliana, A characterization study of the surface acidity of solid catalysts by temperature programmed methods, *Appl. Catal. Gen.* 170 (1998) 127–137, [https://doi.org/10.1016/S0926-860X\(98\)00041-6](https://doi.org/10.1016/S0926-860X(98)00041-6).
- [57] N. Perret, F. Cárdenas-Lizana, M.A. Keane, Selective hydrogenation of benzaldehyde to benzyl alcohol over Au/Al₂O₃, *Catal. Commun.* 16 (2011) 159–164, <https://doi.org/10.1016/j.catcom.2011.09.017>.
- [58] G. Neri, M.G. Musolino, C. Milone, D. Pietropaolo, S. Galvagno, Particle size effect in the catalytic hydrogenation of 2,4-dinitrotoluene over Pd/C catalysts, *Appl. Catal. Gen.* 208 (2001) 307–316, [https://doi.org/10.1016/S0926-860X\(00\)00717-1](https://doi.org/10.1016/S0926-860X(00)00717-1).
- [59] L. Di, J. Zhang, M. Craven, Y. Wang, H. Wang, X. Zhang, X. Tu, Dehydrogenation of formic acid over Pd/C catalysts: insight into the cold plasma treatment, *Catal. Sci. Technol.* 10 (2020) 6129–6138, <https://doi.org/10.1039/D0CY00055H>.
- [60] M. Stucchi, S. Capelli, A. Villa, B.D. Vandegehuchte, L. Prati, Effect of carbon oxygen functionalization on the activity of Pd/C catalysts in hydrogenation reactions, *ChemCatChem* 16 (2024) e202301639, <https://doi.org/10.1002/cctc.202301639>.
- [61] A. Palliyarayil, P. Selvarajan, P.S. Prakash, C.I. Sathish, Venkata.D.B.C. Dasireddy, A. Vinu, N.S. Kumar, S. Sil, An experimental and theoretical investigation on the oxidation of CO over Pd/C derived from the spent Pd catalyst, *ChemCatChem* 13 (2021) 1326–1339, <https://doi.org/10.1002/cctc.202001917>.
- [62] J. Navarro-Ruiz, J. Audevard, M. Vidal, C.H. Campos, I. Del Rosal, P. Serp, I. C. Gerber, Mechanism of hydrogen spillover on metal-doped carbon materials: surface carboxylic groups are key, *ACS Catal.* 14 (2024) 7111–7126, <https://doi.org/10.1021/acscatal.4c00293>.
- [63] H. Yang, R. Nie, W. Xia, X. Yu, D. Jin, X. Lu, D. Zhou, Q. Xia, Co embedded within biomass-derived mesoporous N-doped carbon as an acid-resistant and chemoselective catalyst for transfer hydrodeoxygenation of biomass with formic acid, *Green Chem.* 19 (2017) 5714–5722, <https://doi.org/10.1039/C7GC02648J>.
- [64] R. Huang, C. Cao, J. Liu, L. Zheng, Q. Zhang, L. Gu, L. Jiang, W. Song, Integration of metal single atoms on hierarchical porous nitrogen-doped carbon for highly efficient hydrogenation of large-sized molecules in the pharmaceutical industry, *ACS Applied Materials and Interfaces Journal* 12 (2020) 17651–17658, <https://doi.org/10.1021/acsaami.0c03452>.
- [65] P. Liu, Y. Zhao, R. Qin, S. Mo, G. Chen, L. Gu, D.M. Chevrier, P. Zhang, Q. Guo, D. Zang, B. Wu, G. Fu, N. Zheng, Photochemical route for synthesizing atomically dispersed palladium catalysts, *Science* 352 (2016) 797–800, <https://doi.org/10.1126/science.aaf5251>.
- [66] U. Sanyal, K. Koh, L.C. Meyer, A. Karkamkar, O.Y. Gutiérrez, Simultaneous electrocatalytic hydrogenation of aldehydes and phenol over carbon-supported metals, *J. Appl. Electrochem.* 51 (2021) 27–36, <https://doi.org/10.1007/s10800-020-01464-7>.
- [67] S.A. Akhade, M.-S. Lee, L.C. Meyer, S.F. Yuk, M.-T. Nguyen, U. Sanyal, J.D. Egbert, O.Y. Gutiérrez, V.-A. Glezakou, R. Rousseau, Impact of functional groups on the electrocatalytic hydrogenation of aromatic carbonyls to alcohols, *Catal. Today* 397–399 (2022) 63–68, <https://doi.org/10.1016/j.cattod.2021.11.047>.
- [68] X. Kong, L. Chen, Chemoselective hydrogenation of aromatic aldehydes over SiO₂ modified Co₂/Al₂O₃, *Appl. Catal. Gen.* 476 (2014) 34–38, <https://doi.org/10.1016/j.apcata.2014.02.011>.
- [69] A. Liu, X. Wang, D. Gao, L. Wang, J. Cheng, A. Wang, Z. Zhang, Low temperature chemoselective hydrogenation of aldehydes over a magnetic Pd catalyst, *Appl. Sci.* 9 (2019) 1792, <https://doi.org/10.3390/app9091792>.
- [70] A. Proto, R. Cucciniello, A. Genga, C. Capacchione, A study on the catalytic hydrogenation of aldehydes using mayenite as active support for palladium, *Catal. Commun.* 68 (2015) 41–45, <https://doi.org/10.1016/j.catcom.2015.04.028>.
- [71] M. Stucchi, F. Vasile, S. Cattaneo, A. Villa, A. Chierogato, B.D. Vandegehuchte, L. Prati, An insight into the role of reactant structure effect in Pd/C catalysed aldehyde hydrogenation, *Nanomaterials* 12 (2022) 908, <https://doi.org/10.3390/nano12060908>.
- [72] A. Saadi, Z. Rassoul, M.M. Bettahar, Gas phase hydrogenation of benzaldehyde over supported copper catalysts, *J. Mol. Catal. Chem.* 164 (2000) 205–216, [https://doi.org/10.1016/S1381-1169\(00\)00199-0](https://doi.org/10.1016/S1381-1169(00)00199-0).
- [73] O.B. Belskaya, R.M. Mironenko, V.A. Likhoholov, Effect of carbon support nature and palladium content on the properties of Pd/C catalysts in hydrogenation of benzaldehyde, *Theor. Exp. Chem.* 48 (2013) 381–385, <https://doi.org/10.1007/s11237-013-9285-y>.
- [74] R.M. Mironenko, O.B. Belskaya, T.I. Gulyaeva, M.V. Trenikhin, A.I. Nizovskii, A. V. Kalinkin, V.I. Bukhtiyarov, A.V. Lavrenov, V.A. Likhoholov, Liquid-phase hydrogenation of benzaldehyde over Pd-Ru/C catalysts: synergistic effect between supported metals, *Catal. Today* 279 (2017) 2–9, <https://doi.org/10.1016/j.cattod.2016.07.022>.
- [75] S.F. Yuk, M.-S. Lee, S.A. Akhade, M.-T. Nguyen, V.-A. Glezakou, R. Rousseau, First-principle investigation on catalytic hydrogenation of benzaldehyde over Pt-group metals, *Catal. Today* 388–389 (2022) 208–215, <https://doi.org/10.1016/j.cattod.2020.07.039>.
- [76] T. Zheng, F. Wu, H. Fu, L. Zeng, C. Shang, L. Zhu, Z. Guo, Rational design of Pt–Pd–Ni trimetallic nanocatalysts for room-temperature benzaldehyde and styrene hydrogenation, *Chem. Asian J.* 16 (2021) 2298–2306, <https://doi.org/10.1002/asia.202100472>.
- [77] A. Lazzarini, R. Pellegrini, A. Piovano, S. Rudić, C. Castan-Guerrero, P. Torelli, M. R. Chierotti, R. Gobetto, C. Lamberti, E. Groppo, The effect of surface chemistry on the performances of Pd-based catalysts supported on activated carbons, *Catal. Sci. Technol.* 7 (2017) 4162–4172, <https://doi.org/10.1039/C7CY01005B>.
- [78] Y. Zhang, J. Zhou, K. Li, M. Lv, Synergistic catalysis of hybrid nano-structure Pd catalyst for highly efficient catalytic selective hydrogenation of benzaldehyde, *Catal. Today* 358 (2020) 129–137, <https://doi.org/10.1016/j.cattod.2020.01.022>.
- [79] X. Li, Y. Shen, L. Song, H. Wang, H. Wu, Y. Liu, P. Wu, Efficient hydrogenation of benzaldehydes over mesopolymer-entrapped Pt nanoparticles in water, *Chem. Asian J.* 4 (2009) 699–706, <https://doi.org/10.1002/asia.200800460>.
- [80] Y. Hao, C. Pischetola, F. Cárdenas-Lizana, M.A. Keane, Selective liquid phase hydrogenation of benzaldehyde to benzyl alcohol over alumina supported gold, *Catal. Lett.* 150 (2020) 881–887, <https://doi.org/10.1007/s10562-019-02944-y>.
- [81] Y. Zhang, J. Zhou, F. Wang, M. Lv, K. Li, Metal-metal oxide synergistic catalysis: Pt nanoparticles anchored on mono-layer dispersed ZrO₂ in SBA-15 for high efficiency selective hydrogenation, *J. Catal.* 421 (2023) 12–19, <https://doi.org/10.1016/j.jcat.2023.03.006>.
- [82] T. Fovanna, M. Nachtegaal, A.H. Clark, O. Kröcher, D. Ferri, Preparation, quantification, and reaction of Pd hydrides on Pd/Al₂O₃ in liquid environment, *ACS Catal.* 13 (2023) 3323–3332, <https://doi.org/10.1021/acscatal.2c04791>.
- [83] P.R. Ellis, C.M. Brown, P.T. Bishop, D. Ievlev, J. Yin, K. Cooke, R.E. Palmer, High-selectivity palladium catalysts for the partial hydrogenation of alkenes by gas-phase cluster deposition onto oxide powders, *Catal. Struct. React.* 4 (2018) 1–8, <https://doi.org/10.1080/2055074X.2018.1477315>.